Carbon nanotubes-ferrite-manganese dioxide micromotors for advanced oxidation processes in water treatment†

Roberto Maria-Hormigos [ab], Marta Pacheco [ab], Beatriz Jurado-Sánchez*[ab] and Alberto Escarpa *[ab]

Multifunctional SW-Fe$_2$O$_3$/MnO$_2$ tubular micromotors are used for 'on-the-fly' advanced water oxidation of industrial organic pollutants. Catalytic decomposition of H$_2$O$_2$ as an oxidation agent results in the pro- duction of oxygen bubbles and hydroxyl radicals for complete mineralization of model pollutants into CO$_2$ and H$_2$O. The carbon backbone with Fe$_2$O$_3$ nanoparticles results in a rough catalytic layer for increased speed (16-fold acceleration as compared with smooth counterparts) and a higher radical production rate. The micromotors can propel autonomously in complex wastewater samples (400 µm s^{-1}, 2% H$_2$O$_2$) using a biocompatible surfactant and obviating the need for expensive Pt catalysts. Such self-propelled micro- motors act as highly efficient dynamic oxidation platforms that offer significantly shorter and more efficient water treatment processes, reducing the use of chemical reagents. The effective operation of the SW- Fe$_2$O$_3$/MnO$_2$ micromotors is illustrated towards the oxidative degradation of mg L^{-1} levels of Remazol Brilliant blue and 4-chlorophenol. Factors influencing the micromachine-enhanced oxidation protocol, such as the pH, navigation time and number of motors, have been investigated. High degradation rates of ∼80% are obtained for both pollutants following 60 min treatment of spiked wastewater samples at pH 4.0–5.0.

The unique magnetic properties of the outer Fe$_2$O$_3$ layer allow the reusability of the micromotors and its convenient recovery and disposal after treatment. Such attractive performance holds considerable promise for its application in large scale water treatment systems and for a myriad of environmental, industrial and security defense fields.

Introduction

Water resources, which are vital for the sustainability of life, are directly threatened by anthropogenic activities.[1] The Clean Water Act in the United States and Directive 2013/39/EU of the European Union aimed to govern water pollution by preventing point and nonpoint pollution sources. This resulted in the establishment of maximum allowable levels through a list of priority substances including pesticides, phenols, personal care products, or azo-dyes.[2,3] To adhere to such strict regulations, adequate wastewater management is required either by biological, physical or chemical treatment. Among such treatments, ad- vanced water oxidation is particularly attractive owing to the ef- fectiveness to degrade recalcitrant organic pollutants into non- harmful products like water molecules and carbon dioxide.[4,5] Emerging applications of nanotechnology have added a new dimension to alternative sustainable environmental treatment operations.[6,7] Self-propelled motors, capable of converting energy into movement and forces, are the perfect example of nanomaterials with improved efficiency in water treatment processes.[8–17] Continuous movement of such microscale objects imparts significant mixing without exter- nal stirring, leading to higher efficiencies and shorter clean- up times. Yet, the type of material used in its preparation exert a strong influence in the intended application.[18–20] For example, carbon nanomaterials based micromotors with a catalytic Pt layer have been applied for the absorptive re- moval of heavy metal, azo-dyes, nerve agents and persistent organic pollutant.[21–25] Wang's group illustrated the use of thiol modified Mg micromotors for effective removal of oil droplets or heavy metals.[26,27] Metal oxide based Janus micro- motors based on TiO$_2$ or WO$_3$ layers are extremely effective in photocatalytic degradation schemes.[28–31] Of particular interest, rolled-

up tubular and metal organic framework microengines, comprising Fe as reactive material, can be used for degrading organic pollutants in water *via* the Fenton-like or other degradation mechanism.[32–35] Yet, the above mentioned strategies involve expensive clean-room preparation procedures and/or platinum catalyst, making its widespread use in large scale treatment plants economically less viable. As an alternative, Jänis group proposed the use of manganese dioxide as cost effective catalyst for the prepara- tion of micromotors.[36,37] In addition, such motors are also promising in the advanced oxidation–adsorptive bubble sepa- ration of dyes in water. Yet, the strategy relies on the use of toxic surfactants and the absence of magnetic layers prevent its effective recovery.[38] Sánchez's group recently described surfactant free cobalt-based Janus micromotors for tetracy- cline antibiotics recovery from water *via* Fenton oxidation.[39] Yet, due current increasing demands for cobalt in energy storage applications such material is not economically viable. Herein we describe the synthesis of multifunctional SW-Fe$_2$O$_3$/MnO$_2$ micromotors for advanced water oxidation of an- thraquinone dyes and chlorophenols models in real wastewa- ter samples. Micromotors are prepared by common template electrodeposition involving the simultaneous deposition of a first SW layer containing "trapped" Fe$_2$O$_3$ nanoparticles, followed by the deposition of a second MnO$_2$ catalytic layer. As will be also illustrated, such outer layer imparts the micromotors with magnetic properties for further removal and reusability in water treatment. Catalytic decomposition of H$_2$O$_2$ fuel (which also act as essential reagent) results in the production of oxygen bubbles along with hydroxyl radi- cals for further oxidative degradation of model pollutants (see Fig. 1) into harmless products (CO$_2$ and H$_2$O). The mech- anism behind the Fenton-like reaction of the micromotors re- lies on the catalytic decomposition-conversion of H$_2$O$_2$ into hydroxyl radicals and oxygen in the inner catalytic MnO$_2$ layer. Oxygen microbubbles are ejected from the concave end of the micromotors, initiating its autonomous movement and enhanced fluid mixing while dispersing at the same time the hydroxyl radicals generated for further oxidative degradation of the pollutants. The catalytic MnO$_2$ layer increased both the rate of hydroxyl radical generation and the conversion yield of H$_2$O$_2$.[40] To

mind the gap between proof-of-concept and real environmental applications, we will demonstrate the efficient propulsion of our micromotors using a biocompatible surfactant (Tween 20) at a remarkably high speed of 400 μm s^{-1}. Enhanced micromotor movement along with radical gen- eration results in the complete degradation of mg L^{-1} concentrations Remazol Brilliant blue and 4-chlorophenol after 60 min treatment with the micromotors. Main advantages over previous works is that micromotors can be prepared in ton quantities in a cost-effective way, do not require the use of toxic surfactants, use peroxide as essential reagent and can be reused with negligible lost in the removal efficiency. Such attractive performance holds considerable promise for its ap- plication in large scale wastewater treatment systems, reduc- ing the use of chemical reagents and overall environmental impact through reusability and lower materials requirements and waste generation.

Results and discussion

Fig. 2A illustrate the preparation of SW-Fe$_2$O$_3$/MnO$_2$ tubular micromotors.[41] For control experiments, SW/MnO$_2$ and PEDOT/MnO$_2$ micromotors were prepared in a similar fash- ion. The preparation protocol relies on the simultaneous electrodeposition of the SW carbon outer layer along with the simultaneous entrapment of Fe$_2$O$_3$ nanoparticles, which are also present in the platting solution. Fig. 2B shows the cyclic voltammograms corresponding to the reduction ($n = 1$, 3, and 7 scans) of the Fe$_2$O$_3$ enriched SW layer. Further details on the electrochemical deposition processes can be found in the literature.[41–43] As will be also described later, carbon nanotubes and Fe$_2$O$_3$ nanoparticles exert a strong influence in the average micromotor speed and its performance during environmental processes. The deposition of the second MnO$_2$ layer confers the microtube with structural stability, being also essential for efficient micromotor propulsion and OH$^\cdot$ radical's generation towards pollutants degradation. The resulting micromotors were characterized by SEM and EDX (Fig. 2C), further confirming the presence and uniform distri- bution of C, Fe, Mn and O within the conical micromotors. We further investigate the crystal phases of the nanocatalyst used in our micromotors due to its role in the further cata- lytic performance. Commercial γ-Fe$_2$O$_3$ with a cubic structure have been employed. For MnO$_2$, a very recent paper from Wang's group[44] study the influence of different electrodeposition conditions (potentiodynamic, potentiostatic and galvanostatic) in the fabrication of tubular micromotors using the same precursors we use in this paper. XRD pattern revealed that regardless the deposition mode, there were no differences in the crystal structure of MnO$_2$. Thus, according to this and since we use

similar electrodeposition condi- tions, main crystalline forms in our micromotors are rho- dochrosite MnCO$_3$ and ramsdellite MnO$_2$ (R-MnO$_2$). The latter one has a better performance as catalyst compared to α, β, γ, and ε-MnO$_2$ types, which imparts our micro- motors with high decontamination capabilities. For com- parison, SW/MnO$_2$ micromotors do not contain Fe in its structure.

Prior to test the practical applicability of our micromotors, we studied its propulsion in wastewater and its magnetic properties. The time lapse-microscopy images of Fig. 3 (taken from Video S1†) and corresponding speed profiles illustrate the efficient propulsion of SW-Fe$_2$O$_3$/MnO$_2$ micromotors (middle part) and close-up SEM images of the outer morphol- ogy of the microtubes. A long tail of oxygen bubbles gener- ated from the catalytic decomposition of H$_2$O$_2$ by the rough MnO$_2$ inner layer are released from the rear large-opening side of the micromotors, which reached average speeds of 490 ± 112 μm s^{-1}, in 2% H$_2$O$_2$. Such speed is higher than that observed control PEDOT/MnO$_2$ (30 ± 10 μm s^{-1}) micromotors. This nearly 16-fold acceleration of SW-Fe$_2$O$_3$/MnO$_2$ micro- motors reflects its larger catalytic surface area and enhanced catalytic properties along with improved fuel accessibility. In- deed, SEM images reveal the rough outer morphology of our micromotors results in a rough inner MnO$_2$ layer for im- proved fuel decomposition. This will also result in an in- creased OH$^\cdot$ radicals generation, essential for further pollut- ant degradation. Please note the relatively smooth morphology of control micromotors (particularly PEDOT), which is directly related with its lower catalytic area and di- minished speeds. It should be mentioned here that the speed of SW–MnO$_2$ micromotors was similar to that observed for SW-Fe$_2$O$_3$/MnO$_2$ micromotors. Yet, as will be illustrated in the following section, the magnetic ferrite layer imparts the micromotors with magnetic properties for further reusability schemes with important environmental sustainability impli- cations. In additions, enhanced OH$^\cdot$ radical production rate for more efficient pollutant oxidation. The complete cycle ex- periment for Remazol and 4-chlorophenol degradation is schematically depicted in Fig. S1.

We also compared the effect of different surfactants upon the speed of SW-Fe$_2$O$_3$/MnO$_2$ (see Fig. 3C) micromotors, es- sential for efficient bubble formation and micromotor move- ment. Interestingly, the highest speeds were noted using Tween 20 (0.5%) as surfactant, which was then selected for further decontamination experiments. To the best of our knowledge, this is the first time that a biocompatible surfactant is used in connection with micromotors in environmental studies, overcoming some of the problems encountered for the application of such tiny counterparts in the field. An- other important aspect for such applications is the possibility to confer the micromotors with magnetic properties for further reusability and adequate removal-disposal schemes. The Fe$_2$O$_3$ nanoparticles in the inner carbon layer are responsible for the direct navigation of a micromotor toward an area with a high magnetic field, as well as the efficient control of its navigation using a magnet (see Fig. 4 and Video S2†). The stability of Fe$_2$O$_3$ and MnO$_2$ towards peroxide corrosion was evaluated by performing EDX mapping of the distribution of such elements in the

micromotors before and after 60 min navigation in 2% H_2O_2 solution. Images of Fig. 4C indicate that elements distribution remains unaltered, which is an- other advantage of our micromotors in subsequent environ- mental applications.

As a first proof-of-concept application, we examined the ability of our SW-Fe_2O_3/MnO_2 micromotors for the degradation of Remazol Brilliant Blue R (λ_{max} = 590 nm), an anthraquinone dye widely used in industry at high quantities. To prove the presence of OH$^{.}$ radicals, we performed a colorimetric assay with 2,2-azino-bis·3-ethylbenzothiazoline-6- sulfonate) (ABTS). ABTS display strong adsorption at 340 nm with a molar extinction coefficient ϵ_{340} of 3.6×10^4 $M^{-1}cm^{-1}$.

On oxidation under the presence of OH$^{.}$ radicals mainly, ABTS forms a stable blue-green product presumed to be the cation radical, $ABTS^{+.}$, which can be conveniently followed at λ_{max} at 415 nm (ϵ_{415} = 3.6×10^4 M^{-1} cm^{-1}). Thus, an experiment was carried out by mixing ABTS (0.25 mM) with hydro gen peroxide (5 mM) and the SW-Fe_2O_3/MnO_2 micromotors solution in acetate buffer solution (0.025 M, pH 4). The absorbance was recorded during 300 s at a wavelength of 415 nm. A clear absorption band which has a maximum absorbance at 415 nm, which correlates well with the characteristic absorption peak oxidation product of ABTS, with a typical green color, indicative of the production of OH$^{.}$ radicals, was observed. Such results agree with a very recent research paper from our group on th use of this micromotors for detection of isomeric compounds based on OH$^{.}$ radical production by the micromotors.[45]

We first evaluated the effect of time and number of motors upon degradation (see Fig. 5B). To this end, 10 mL wastewater aliquots were fortified with the pollutant (C_0 = 19 mg L^{-1}) and surfactant (Tween 20, 0.5%). After peroxide addition (1%) sample aliquots were taken at different times and the extent of removal was monitored by the decrease of its typical absorbance peak (590 nm) by UV-vis spectrophotometry. Experiments were performed with 1% peroxide levels, so the real concentration is closer to that used in real Fenton reactions. Lowering the peroxide level will decrease also the overall cost of this proof-of-concept application. Degradation rates increases as the number of motors and time increase, reaching a maximum of 80% removal using 1.5×10^6 motors mL^{-1} for 30 min. As the weight of a micromotor was estimated to be 40 ng, this amount corresponds to a total weight of 60 mg. Initial pH of wastewater was adjusted to 7 (when applicable) as can be seen in Fig. S2, after Remazol addition, pH drops down to 3.8, followed by a rapid increase to pH 4.8 (after 10 min) and then remained constant. Next, the impact of pH on the degradation efficiency was studied at pH 7.0 and 10.0 by adjusting it to after Remazol addition with phosphate or ammonia buffer. At such conditions, negligible degradation rates were noted, as compared with pH 4.0–5.0. At acidic pH, excess H$^+$ ions in solution induce a positive charge on catalyst surface, enhancing both adsorption and catalytic oxidation *via* electrostatic attraction, taking into ac- count the anionic nature of the reactive dye in solution. In basic medium, hydrogen peroxide dissociates into H$^+$ ions and perhydroxyl anions. Thus, acidic pH enhances the formation of extremely reactive hydroxyl radical and thus the oxidation efficiency.[46,47] Such hydroxyl radical can attack carbon bonds in remazol structure, leading to its complete mineralization into non-harmful products.[47] We next investigate the mineralization of RBB by the micromotors by evaluating the total organic car- bon (TOC) removal percentages (for further details, see Table S1 and Experimental section), which were around 61%. Such results indicate that effective mineralization of RBB occurs after treatment with SW-Fe_2O_3/MnO_2 micromotors.

Several control experiments were next performed. Slightly lower degradation rates of 70% (not shown) were obtained with SW$-MnO_2$, which revealed the role of ferrite nano-particles in enhanced OH$^{.}$ radicals production. Thus, H_2O_2 is a Lewis base with a strong affinity for surface-confined fer-rous ions. Thus, a complex between the "trapped" ferrite nanoparticles and H_2O_2 is generated. Due to such entrap-ment, electron transfer to the H_2O_2, resulting in the genera-tion of ferrous ion and additional OH$^{.}$ radicals input to further oxidize the pollutants.[48] In control experiments performed using static SW-Fe_2O_3/MnO_2 (under the absence of H_2O_2) negligible remazol degradation was noted (see Fig. 5C), probably due to the absence of hydroxyl radicals which are directly responsible for such degradation. Similar findings were encountered using moving SW/PtNPs micromotors, which indicates an additional effect of MnO_2 catalyst over Pt, probably to a remazol-mediated interaction with the catalyst, as similarly reported.[38] In addition, catalytic activities of Pt catalyst can be modulated by the pH value of the environ-ment. Thus, Pt display peroxidase-like activity, decomposing H_2O_2 into OH$^{.}$ under acidic conditions (1.1–3.6), but catalase-like activity of producing H_2O and O_2 under nearly neutral and alkaline conditions (4.0–12.0).[49] Such low OH$^{.}$ radical's generation result nearly negligible degradation rates. For PEDOT/MnO_2 micromotors, lower degradation rates of ~38% were obtained due to its lower catalytic area and hydroxyl radical production. We perform additional control experi-ments using MnO_2 (300 nm) and Fe_2O_3 (50 nm) nano-particles as static catalyst. The latter can be used also to com-pare the efficiency of our micromotors with the homogeneous Fenton system. Released iron concentration was just 1.8 μg L^{-1} from a 1.5×10^6 micromotors mL^{-1} dispersion after 1 hour of swimming in 2% H_2O_2, whereas the batch of micromotors contains 1982 μg L^{-1} of iron. As can be seen, the amount of iron present in solution is negligible as compared with the amount present in the micromotors. On both cases, degradation rates of ~30% were obtained. Please also note here that some authors have described the autonomous motion of MnO_2 nanoparticles in peroxide solutions, inducing enhanced movement responsible for such degradation rates of such catalyst.[38] Yet, the engineered structure and magnetic properties of our micromotors allow for recovery after water treatment and future reusability over consecutive cycles. Percent degradation were 82 and 75% on the first a second cycle, respectively, holding thus considerable poten- tial in future full-scale applications. Negligible degradation rates were obtained with MnO_2 and/or Fe_2O_3 nanoparticles in a second cycle (lower than 10%), maybe due to the absence of

magnetic properties to confine the nanoparticles, avoiding their lost in solution which is the main advantage of our micromotor.

Finally, to get further insights into the mechanisms re-sponsible for RBB degradation using SW-Fe$_2$O$_3$/MnO$_2$ micro-motors, data from effect of time on the removal of such pol-lutant using the optimal conditions was processed under two common kinetic models (pseudo-first-order and pseudo-second-order). Details on the calculation are described in the Experimental section. The plots of Fig. 5D and E illustrate that the data do not fit well to the pseudo-first-order model, with a correlation coefficient of 0.923 and adjust better with the pseudo-second order model (correlation coefficient, 0.992). Corresponding UV-vis spectra changes can be found in Fig. S3. Such data indicate that RBB degradation follows a mix advanced oxidation–adsorptive bubble degradation mechanism as previously reported for MnO$_2$ catalytic motors.[38]

In a second application, we evaluated our micromotors in the degradation of 4-chlorophenol, a model pesticide. The proposed degradation mechanism, as shown in Fig. 6A, is also triggered by OH$^\cdot$ radicals attack upon carbon bonds in the molecule, generating hydroquinone intermediates which further degrade into non-harmful products.[49] As in the previ-ous case, 10 mL wastewater aliquots (pH 7.0) were fortified with the pollutant (C_0 = 60 mg L^{-1}) and surfactant (Tween 20, 0.5%) and the extent of degradation was monitored by UV-vis (by decrease of the maximum absorbance peak at 285 nm). Experiments were performed with 1% peroxide levels, so the real concentration is closer to that used in real Fenton reactions. Judicious optimization of the time and number of micromotors revealed that 80% percent degradation can be achieved treating the water with 1 × 10^6 motors mL^{-1} (40 mg of micromotors) for 60 min.

As in the previous case, initial pH of wastewater was adjusted to 7.0 (when applicable) and after 4-chlorophenol addition (see Fig. S2†) a rapid pH drops down to pH 4.8 was noted, followed by a fast increase to pH 5.4 (after 5 minutes) and a slight decrease until pH 5.0 is reached (20–60 minutes). Next, the impact of pH on the degradation efficiency was studied at pH 7.0 and 10.0 by adjusting it to after 4-chlorophenol addition with phosphate or ammonia buffer. At such conditions, negligible degradation rates were noted, which can be attributed to H$^+$ ions and perhydroxyl anions.[50] As in the case of remazol, slightly lower degradation rates of 65% (not shown) were obtained with SW–MnO$_2$, due probably also to enhanced OH$^\cdot$ radical's generation by ferrite nanoparticles. TOC removal percentages

(for further details, see Table S1 and Experimental section) of around 61% were obtained, which further indicate that effective mineralization of 4-CP occurs after treatment with SW-Fe$_2$O$_3$/MnO$_2$ micromotors. Under optimal conditions, control experiments were performed with static SW-Fe$_2$O$_3$/MnO$_2$ (under the absence of H$_2$O$_2$), SW-Fe$_2$O$_3$/MnO$_2$ micromotors under magnetic stirring or moving SW/PtNPs, obtaining negligible degradations rates. For PEDOT/MnO$_2$ micromotors such rates are even lower than in the case of remazol (20%) due to its lower catalytic activity and OH$^\cdot$ radicals generation. Also, excellent removal percentages were obtained in reusability experiments, with 80 and 78% degradation rates in the first and second cycle, respectively. As in the previous case, low degradation rates were obtained for MnO$_2$ nanoparticles (35%) as static catalyst. Yet, very low degradation rate of 18% was noted for Fe$_2$O$_3$ (50 nm) nanoparticles. In addition, reusability test performed at 1% and 2% peroxide levels revealed the poor reusability properties of MnO$_2$ nanoparticles (maybe due to the absence of magnetic properties to confine the nanoparticles, avoiding their lost in solution) with degradation rates lower than 10% in a second degradation cycle.

To get further insights into the mechanisms responsible for 4-CP degradation using SW-Fe$_2$O$_3$/MnO$_2$ micromotors, data from effect of time on the removal of such pollutant using the optimal conditions was processed under two com-mon kinetic models (pseudo-first-order and pseudo-second-order). The plots of Fig. 6C and D illustrate that the data fit well to the pseudo-first-order model, with a correlation coeffi-cient of 0.961, whereas it do not fit the pseudo-second order model. For corresponding UV-vis spectra, see Fig. S3.

Conclusions

We have demonstrated the use of multifunctional SW-Fe$_2$O$_3$/MnO$_2$ micromotors for the advanced oxidation of industrial organic pollutants in real wastewater samples. Micromotors can be mass-prepared by template electrochemical deposi-tion, obviating the need for expensive Pt catalysts or clean-room procedures. Catalytic decomposition of H$_2$O$_2$ by the MnO$_2$ fuel catalytic layer results in the production of oxygen bubbles along with hydroxyl radicals for environmental friendly degradation of the model pollutants. The incorporation of Fe$_2$O$_3$ and the carbon backbone impart the micromotors defects and edges, resulting in a rough catalytic layer for increased speeds (16-fold acceleration as compared with smooth counterparts) and higher hydroxyl production rate for improved pollutant degradation. Thus, the micromotors can propel autonomously in complex wastewater samples using Tween 20 as environmental friendly surfactant at bout 400 μm s−1 (2% H$_2$O$_2$), holding considerable promise for full scale applications. The practical utility of our micromotors have been demonstrated for the oxidative degradation of mg−1 levels of Remazol Brilliant blue and 4-chlorophenol. Enhanced micromotor movement along with radical generation results in high degradation rates of ~80% for both pollutants after 60 min treatment of spiked wastewater samples. The unique magnetic properties of the outer Fe2O3 layer allow the reusability of the micromotors, with negligible decrease in the degradation rates after a second operation cycle. Similar efficiencies have been recently reported using metal sulfides as co-catalysts or graphene

oxide hydrogels to increase H_2O_2 decomposition and overall performance in Fenton reactions for azo dye degradation.[51,52] This have been also achieved with hematite and goethite nanocrystals in connection with ascorbic acid and hydrogen peroxide.[53–57] Such attractive performance also holds considerable promise for its application in a myriad of environmental, industrial and security defense applications. Compared to previous works,[21,23,32,33,38,39] our micromotors can be prepared in ton quantities in a cost-effective way, do not require the use of toxic surfactants, use peroxide as essential reagent and can be reused with negligible lost in the removal efficiency. Such attractive performance holds considerable promise for its application in large scale wastewater treatment systems, reducing the use of chemical reagents and overall environmental impact through reusability and lower materials requirements and waster generation. Yet, more improvements are still needed to address scalability of motor production and toward operation in large water volumes and full-scale water treatment plants.

Experimental

Reagents and equipment

Carboxylic functionalized single-walled carbon nanotubes (SWCNTs-COOH, 0.7–1.3 nm diameter, cat. 704113), iron(ɪɪɪ) oxide (nanopowder, <50 nm particle size, cat. 544884), 3,4-ethylenedioxythiophene (EDOT, cat. 483028), poly (sodium 4-styrene sulphonate) (PSS, cat. 243051), manganese(ɪɪ) ace- tate tetra-hydrate (cat. 229776), chloroplatinic acid (cat. 520896), boric acid (cat. 202878), sodium sulfate (cat. 204447), sodium cholate hydrate (cat. C6445), Tween 20 (cat. P9416), hydrogen peroxide (cat. 216763), 2,2′-azino-bis(3- ethylbenzothiazoline-6-sulfonic acid) diammonium salt, ABTS (cat. A1888), Remazol Brilliant Blue R (cat. R8001) and 4-chlorophenol (cat. 35826) were obtained from Sigma- Aldrich. Sodium dodecyl sulfate (cat. 71727) were supplied by Merck (Germany). MnO_2 nanoparticles were synthetized in our lab following a previously described procedure.[58] In brief, 2 mL of 6 M HCl was added dropwise to 10 mL of 0.1 M $KMnO_4$. The mixture was stirred for 5 min at room tempera- ture. The resulting MnO_2 microparticles were washed five times with deionized water, and then dried in air at room temperature for 24 h.[58]

Micromotors synthesis was carried out using an Autolab PGSTAT 12 (Eco Chemie, Utrecht, The Netherlands). SEM and EDX images were obtained with a Jeol JSM 6335F instru- ment using an acceleration voltage of 10 kV. Micromotor movement and speed was tracked by using an inverted opti- cal microscope (Nikon Eclipse Instrument Inc. Ti-S/L100), coupled with 20× objectives, and a Photometrics QuantEM 512/SC (Roper Scientific, Duluth, GA). UV-vis experiments were carried out using a Perkin-Elmer Lambda 20 spectrophotometer. Iron was determined by graphite furnace atomic absorption spectrometry using a continuous source (Analytik Jena, Alemania) and the 248.327 nm and 248.419 nm resonance lines.

Micromotor synthesis

SW-Fe_2O_3/MnO_2, SW/MnO_2 and PEDOT/MnO_2 micromotors were prepared by electrochemical deposition of the different materials into the 2 μm-diameter conical pores of a polycarbonate membrane (Cat. No. 70602511; Whatman, New Jersey, USA). For Fe_2O_3-SW/MnO_2 micromotors, simultaneous electrochemical reduction–deposition and nanoparticles entrapment was carried out using cyclic voltammetry (CV, over +0.3 to −1.5 V vs. Ag/AgCl, 3 M, at 50 mV s^{-1}, for 7 cycles) from a platting solution containing 0.1 mg mL^{-1} of the nanotubes, 5 mg mL^{-1} of Fe_2O_3 and 0.5 M of Na_2SO_4 in 0.1 M H_2SO_4. Next, the inner catalytic inner MnO_2 layer was amperometrically deposited at 0.75 V for 1.3 C from aqueous solution containing 0.01 M manganese) acetate tetrahydrate. For SW/MnO_2 micromotors, same conditions were used by obviating Fe_2O_3 nanoparticles addition in the plat- ting solution. For SW–Pt, the inner PtNPs layer was deposited by amperometry at −0.4 V for 750 s from an aqueous solution containing 4 mM of H_2PtCl_6 in 0.5 M boric acid. PEDOT microtubes were electropolymerized at 0.80 V using a charge of 4 C from a 10 mL plating solution containing 10 mM of EDOT and 125 mM of PSS, followed by platting of the MnO_2 layer. In all cases, sputtered gold layer was removed by hand- polishing and the micromotors were released from the mem- brane by sequential treatment with methylene chloride (30 min, 2 times), isopropanol, ethanol, and ultrapure water (18.2 Ω cm), with 3 min centrifugation following each wash.

Pseudo first order and pseudo second order kinetics

Kinetics studies were carried using with a concentration of 19 or 60 mg L^{-1} of RBB of 4-CP, respectively, at the optimal conditions described in the degradation experiments. Samples were collected at preselected time intervals (5, 10, 20, 25, 30 and 60 min) and the concentration of each pollutant measured.

Pseudo-first-order kinetics were calculated according to the equation:

$$\ln \frac{C_0}{C} = kt$$

where C_0 and C are the concentration of each pollutant in solution at initial and any time t, k is the reaction rate constant and t the specific time. The model was evaluated by plotting the ln(C$_0$/C) $versus$ time.

Pseudo-second-order kinetics were expressed as:

$$\frac{t}{q} = \frac{1}{k\,q^2} + \frac{t}{q}$$

Micromotor propulsion experiments

To evaluate the speed of the micromotors in different environmental media, a glass slide was placed on top of the microscope objective and then 1 μL of each sample (ultrapure or wastewater), surfactant (SDS, sodium cholate or Tween 20) and H_2O_2 solutions were dropped onto the glass slide (total volume, 3 μL). To avoid sample dilution, the different solutions were prepared in wastewater. Video acquisition was started after 30 s peroxide addition. NIS element software was used to track the speed of the micromotors under the different conditions.

Degradation experiments

10 mL of wastewater samples-containing 0.5% of Tween 20-contaminated with of Remazol Brilliant blue (C_0 = 19 mg L^{-1}) or 4-chlorophenol (C_0 = 60 mg L^{-1}), respectively were mixed with a known number of Fe_2O_3-SW/MnO_2 (60 and 40 mg for remazol and 4-chlorophenol experiments, respectively) or control micromotors (60 and 40 mg for remazol and 4-chlorophenol experiments, respectively) and H_2O_2 (1%). The same amount of catalyst and conditions were used for experiments using nanoparticles (MnO_2 or Fe_2O_3). The extent of Remazol or 4-chlorophenol degradation was monitored by taking aliquots at different times and measuring the decrease of their corresponding absorbance signal (590 and 285 nm for remazol and 4-chlorophenol, respectively). For reutilization experiments, micromotors were confined in the bottom of the centrifuge tubes with a magnet, followed by removal of the wastewater solution by gentle pipetting. Prior the next degradation cycle, micromotor were washed with ultrapure water.

where k_2 is the reaction rate constant and q_e and q_t refer to the amount of pollutant present at equilibrium and at time t, respectively. The amount of adsorption at time t, q_t was calculated by:

$$q_t = \frac{V(C_0 - C)}{m}$$

C_0 and C are the concentration of each pollutant in solution at initial and any time t, respectively. V is the volume of the solution (10 mL) and m is the mass micromotors used (60 and 40 mg for RBB and 4-CP, respectively). The model was evaluated by plotting the $t/q_t\ versus$ time.

Conflicts of interest

There are no conflicts to declare.

Acknowledgements

Notes and references

1 C. J. Vorosmarty, P. B. McIntyre, M. O. Gessner, D. Dudgeon, A. Prusevich, P. Green, S. Glidden, S. E. Bunn, C. A. Sullivan, C. R. Liermann and P. M. Davies, Global threats to human water security and river biodiversity, *Nature*, 2010, 467, 555–561.

2 Clean water act, US Environmental Protection Agency, https://www.epa.gov/laws-regulations/summary-clean-water-act.

3 Directive 2013/39/EU of the European Parliament and of the council, http://eur-lex.europa.eu/eli/dir/2013/39/oj.

4 F. C. Moreira, R. A. R. Boaventura, E. Brillas and V. J. P. Vilar, Electrochemical advanced oxidation processes: a review on their application to synthetic and real wastewaters, *Appl. Catal., B*, 2017, 202, 217–261.

5 A. R. Ribeiro, O. C. Nunes, M. F. Pereira and A. M. Silva, An overview on the advanced oxidation processes applied for the treatment of water pollutants defined in the recently launched Directive 2013/39/EU, *Environ. Int.*, 2015, 75, 33–51.

6 M. M. Khin, A. S. Nair, V. J. Babu, R. Murugan and S. Ramakrishna, A review on nanomaterials for environmental remediation, *Energy Environ. Sci.*, 2012, 5, 8075–8109.

7 P. G. Tratnyek and R. L. Johnson, Nanotechnologies for environmental cleanup, *Nano Today*, 2006, 1, 44–48.

8 G. A. Ozin, I. Manners, S. Fournier-Bidoz and A. Arsenault, Dream nanomachines, *Adv. Mater.*, 2005, 17, 3011–3018.

9 S. Sánchez and M. Pumera, Nanorobots: The ultimate wireless self-propelled sensing and actuating devices, *Chem. – Asian J.*, 2009, 4, 1402–1410.

10 A. A. Solovev, Y. Mei, E. Bermúdez Ureña, G. Huang and O. G. Schmidt, Catalytic microtubular jet engines self-propelled by accumulated gas bubbles, *Small*, 2009, 5, 1688–1692.

11 S. J. Ebbens and J. R. Howse, In pursuit of propulsion at the nanoscale, *Soft Matter*, 2010, 6, 726–738.

12 Y. Mei, A. A. Solovev, S. Sánchez and O. G. Schmidt, Rolled-up nanotech on polymers: from basic perception to self-propelled catalytic microengines, *Chem. Soc. Rev.*, 2011, 40, 2109–2119.

13 S. Sengupta, M. E. Ibele and A. Sen, Fantastic voyage: designing self-powered nanorobots, *Angew. Chem., Int. Ed.*, 2012, 51, 8434–8445.

14 J. Wang, *Nanomachines: Fundamentals and Applications*, Wiley, 2013, ISBN: 978-3-527-33120-8.

15 W. Wang, T. Y. Chiang, D. Velegol and T. E. Mallouk, Understanding the efficiency of autonomous nano-and microscale motors, *J. Am. Chem. Soc.*, 2013, 135, 10557–10565.

16 K. Kim, J. Guo, X. Xu and D. L. Fan, Recent progress on man-made inorganic nanomachines, *Small*, 2015, 11, 4037–4057.

17 E. Karshalev, B. Esteban-Fernandez de Avila and J. Wang, Micromotors for "Chemistry-on-the-Fly", *J. Am. Chem. Soc.*, 2018, 140, 3810–3820.

18 B. Jurado-Sánchez and J. Wang, Micromotors for environmental applications. A review, *Environ. Sci.: Nano*, 2018, 5, 1530–1544.

19 L. Soler and S. Sánchez, Catalytic nanomotors for environmental monitoring and water remediation, *Nanoscale*, 2014, 6, 7175–7182.

20 H. Ye, G. Ma, J. Kang, H. Sun and S. Wang, Pt-Free microengines at extremely low peroxide levels, *Chem. Commun.*, 2018, 54, 4653–4656.

21 B. Jurado-Sánchez, S. Sattayasamitsathit, W. Gao, L. Santos, Y. Fedorak, V. V. Singh, J. Orozco, M. Galarnyk and J. Wang, Self-propelled activated carbon Janus micromotors for efficient water purification, *Small*, 2015, 11, 499–506.

22 V. V. Singh, A. Martin, K. Kaufmann, S. D. S. de Oliveira and J. Wang, Zirconia/graphene oxide hybrid micromotors for selective capture of nerve agents, *Chem. Mater.*, 2015, 27, 8162–8169.

23 D. Vilela, J. Parmar, Y. Zeng, Y. Zhao and S. Sánchez, Graphene-based microbots for toxic heavy metal removal and recovery from water, *Nano Lett.*, 2016, 16, 2860–2866.

24 J. Orozco, L. A. Mercante, R. Pol and A. Merkoci, Graphene-based Janus micromotors for the dynamic removal of pollutants, *J. Mater. Chem. A*, 2016, 4, 3371–3378.

25 J. García-Torres, A. Serrà, P. Tierno, X. Alcobé and E. Vallés, Magnetic propulsion of recyclable catalytic nanocleaners for pollutant degradation, *ACS Appl. Mater. Interfaces*, 2017, 9, 23859–23868.

26 W. Gao, X. Feng, A. Pei, Y. Gu, J. Li and J. Wang, Seawater-driven magnesium-based Janus micromotors for environmental remediation, *Nanoscale*, 2013, 5, 4696–4700.

27 D. A. Uygun, B. Jurado-Sánchez, M. Uygun and J. Wang, Self-propelled chelation platforms for efficient removal of toxic metals, *Environ. Sci.: Nano*, 2016, 3, 559–566.

28 J. Li, V. V. Singh, S. Sattayasamitsathit, J. Orozco, K. Kaufmann, R. Dong, W. Gao, B. Jurado-Sánchez, Y. Fedorak and J. Wang, Water-driven micromotors for rapid photocatalytic degradation of biological and chemical warfare agents, *ACS Nano*, 2014, 8, 11118–11125.

29 Y. Wu, R. Dong, Q. Zhang and B. Ren, Dye-enhanced self-electrophoretic propulsion of light-driven TiO2–Au Janus micromotors, *Nano-Micro Lett.*, 2017, 9, 30.

30 Q. Zhang, R. Dong, Y. Wu, W. Gao, Z. He and B. Ren, Light-Driven Au-WO3@C Janus Micromotors for Rapid Photodegradation of Dye Pollutants, *ACS Appl. Mater. Interfaces*, 2017, 9, 4674–4683.

31 S. Wang, Z. Jiang, S. Ouyang, Z. Dai and T. Wang, Internally/Externally Bubble-Propelled Photocatalytic Tubular Nanomotors for Efficient Water Cleaning, *ACS Appl. Mater. Interfaces*, 2017, 9, 23974–23982.

32 J. Parmar, D. Vilela, E. Pellicer, D. Esqué-de los Ojos, J. Sort and S. Sánchez, Reusable and long-lasting active microcleaners for heterogeneous water remediation, *Adv. Funct. Mater.*, 2016, 26, 4152–4161.

33 L. Soler, V. Magdanz, V. M. Fomin, S. Sánchez and O. G. Schmidt, Self-propelled micromotors for cleaning polluted water, *ACS Nano*, 2013, 7, 9611–9620.

34 R. Wang, W. Guo, X. Li, Z. Liu, H. Liu and S. Ding, Highly efficient MOF-based self-propelled micromotors for water purification, *RSC Adv.*, 2017, 7, 42462–42467.

35 S. K. Srivastava, M. Guix and O. G. Schmidt, Wastewater mediated activation of micromotors for efficient water cleaning, *Nano Lett.*, 2016, 16, 817–821.

36 M. Safdar, T. D. Minh, N. Kinnunen and J. Jänis, Manganese oxide based catalytic micromotors: effect of polymorphism on motion, *ACS Appl. Mater. Interfaces*, 2016, 8, 32624–32629.

37 M. Safdar, O. M. Wani and J. Jänis, Manganese oxide-based chemically powered micromotors, *ACS Appl. Mater. Interfaces*, 2015, 7, 25580–25585.

38 O. M. Wani, M. Safdar, N. Kinnunen and J. Jänis, Dual effect of manganese oxide micromotors: catalytic degradation and adsorptive bubble separation of organic pollutants, *Chem. – Eur. J.*, 2016, 22, 1244–1247.

39 J. Parmar, K. Villa, D. Vilela and S. Sánchez, Platinum-free cobalt ferrite based micromotors for antibiotic removal, *Appl. Mater. Today*, 2017, 9, 605–611.

40 S. H. Do, B. Batchelor, H. K. Lee and S. H. Kong, Hydrogen peroxide decomposition on manganese oxide (pyrolusite): Kinetics, intermediates, and mechanism, *Chemosphere*, 2009, 8–12.

41 R. Maria-Hormigos, B. Jurado-Sánchez, L. Vazquez and A. Escarpa, Carbon allotrope nanomaterials based catalytic micromotors, *Chem. Mater.*, 2016, 28, 8962–8970.

42 A. Martin, J. Hernandez-Ferrer, L. Vazquez, M. T. Martinez and A. Escarpa, Controlled chemistry of tailored graphene nanoribbons for electrochemistry: a rational approach to optimizing molecule detection, *RSC Adv.*, 2014, 4, 132–139.

43 K. Wu and S. Hu, Deposition of a thin film of carbon nanotubes onto a glassy carbon electrode by electropolymerization, *Carbon*, 2004, 42, 3237–3242.

44 W. Liu, H. Ge, Z. Gu, X. Lu, J. Li and J. Wang, Electrochemical deposition tailors the catalytic performance of MnO$_2$-based micromotors, *Small*, 2018, 14, 182771.

45 R. María-Hormigos, B. Jurado-Sánchez and A. Escarpa, Self-propelled micromotors for naked-eye detection of phenylenediamines isomers, *Anal. Chem.*, 2018, 90, 9830–9837.

46 N. A. Fathy, S. E. El-Shafey, O. I. El-Shafey and W. S. Mohamed, Oxidative degradation of RB19 dye by a novel g-MnO$_2$/MWCNT nanocomposite catalyst with H$_2$O$_2$, *J. Environ. Chem. Eng.*, 2013, 1, 858–864.

47 K. Omar, Catalytic decomposition of hydrogen peroxide on manganese dioxide nanoparticles at different pH values, *Int. J. Res. Eng. Technol.*, 2014, 2, 241–248.

48 X. Huang, X. Hou, J. Zhao and L. Zhang, Hematite facet confined ferrous ions as high efficient Fenton catalysts to degrade organic contaminants by lowering H$_2$O$_2$ decomposition energetic span, *Appl. Catal., B*, 2016, 181, 127–137.

49 Y. Liu, H. Wu, M. Li, J. J. Yin and Z. Nie, pH dependent catalytic activities of platinum nanoparticles with respect to the decomposition of hydrogen peroxide and scavenging of superoxide and singlet oxygen, *Nanoscale*, 2014, 6, 11904–11910.

50 A. Zhihui, Y. Peng and L. Xiaohua, Degradation of 4-Chlorophenol by microwave irradiation enhanced advanced oxidation processes, *Chemosphere*, 2005, 60, 824–827.

51 M. Xing, W. Xu, C. Dong, Y. Bai, J. Zeng, Y. Zhou, J. Zhang and Y. Yin, Metal sulfides as excellent co-catalysts for H$_2$O$_2$ decomposition in advanced oxidation processes, *Chem*, 2018, 4, 1–14.

52 C. Dong, J. Lu, B. Qiu, B. Shen, M. Xing and J. Zhang, Developing stretchable and graphene-oxide-based hydrogel for the removal of organic pollutants and metal ions, *Appl. Catal., B*, 2018, 222, 146–156.

53 X. Hou, X. Huang, Z. Ai, J. Zhao and L. Zhang, Ascorbic acid/Fe@Fe$_2$O$_3$: A highly efficient combined Fenton reagent to remove organic contaminants, *J. Hazard. Mater.*, 2016, 310, 170–178.

54 X. Hou, X. Huang, F. Jia, Z. Ai, J. Zhao and L. Zhang, Hydroxylamine promoted goethite surface fenton degradation of organic pollutants, *Environ. Sci. Technol.*, 2017, 51, 5118–5126.

55 X. Huang, X. Hou, F. Jia, F. Song, J. Zhao and L. Zhang, Ascorbate-promoted surface iron cycle for efficient heterogeneous fenton alachlor degradation with hematite nanocrystals, *ACS Appl. Mater. Interfaces*, 2017, 9, 8751–8758.

56 X. Hou, X. Huang, M. Li, Y. Zhang, S. Yuan, Z. Ai, J. Zhao and L. Zhang, Fenton oxidation of organic contaminants with aquifer sediment activated by ascorbic acid, *Chem. Eng. J.*, 2018, 348, 255–262.

57 X. Huang, X. Hou, X. Zhang, K. M. Rosso and L. Zhang, Facet-dependent contaminant removal properties of hematite nanocrystals and their environmental implications, *Environ. Sci.: Nano*, 2018, 5, 1790–1806.

58 T. D. Dang, M. A. Cheney, S. Qian, S. W. Joo and B. K. Min, A novel rapid one-step synthesis of manganese oxide nanoparticles at room temperature using poly(dimethylsiloxane), *Ind. Eng. Chem. Res.*, 2013, 52, 2750–2753.

Fig. 1 Schematic representation of the micromotors based advanced oxidation of anthraquinone dyes and chlorophenols into environmentally friendly products and related radical's generation mechanism. Please note that Mn^{2+} represent an intermediate of the reaction that occurs in the surface of the catalyst. As such, Mn^{2+} is not released in solution.
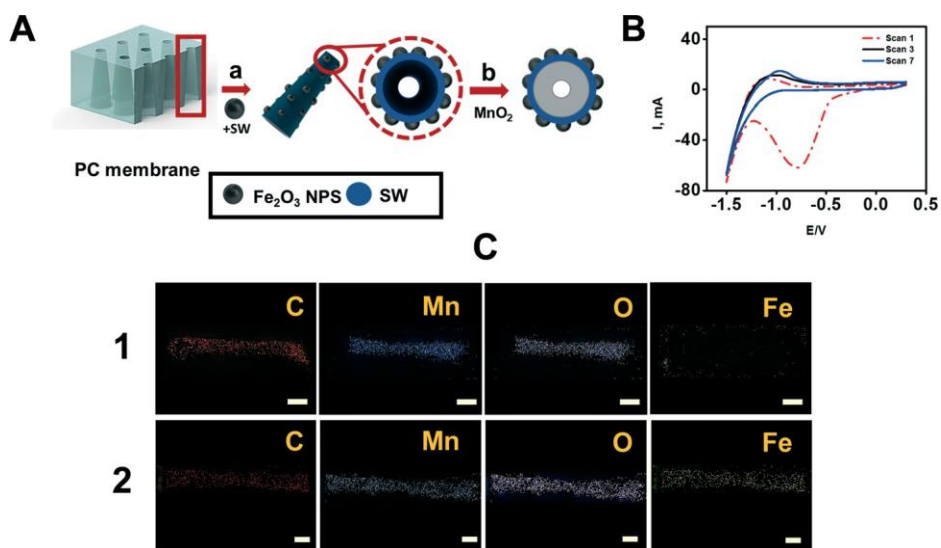

Fig. 2 (A) Schematic of the fabrication of the SW-Fe_2O_3/MnO_2 tubular micromotors. (a) Electrochemical deposition of a SW layer containing the Fe_2O_3 nanoparticles (b) deposition of a catalytic MnO_2 layer. (B) Cyclic voltammograms corresponding to the electrochemical reduction of SW layer. (C) Energy-dispersive X-ray mapping showing the distribution of C, Mn, O and Fe in a (1) SW/MnO_2 and a (2) SW-Fe_2O_3/MnO_2 micromotor. Scale bars, 2 μm.
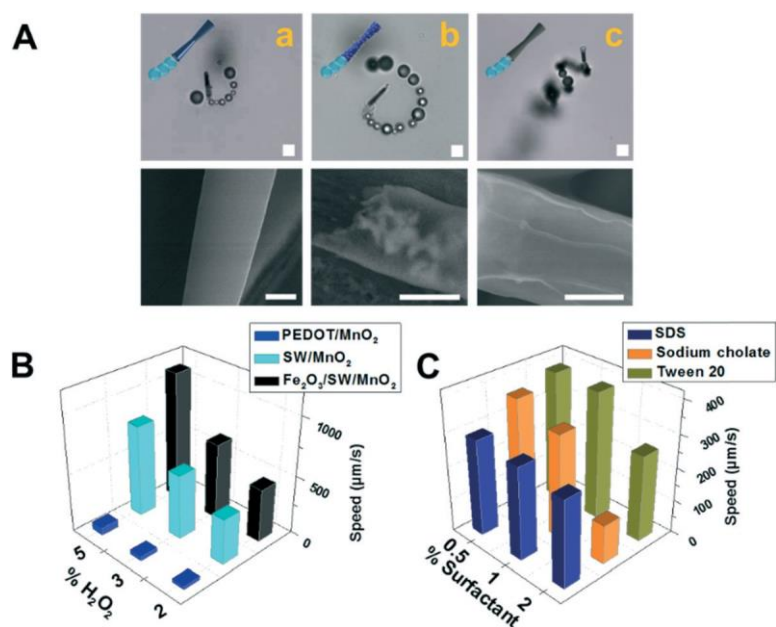
Fig. 3 Catalytic propulsion of SW-Fe$_2$O$_3$/MnO$_2$ micromotors. (A) Time-lapse microscopy images (taken from Video S1†) of the efficient propulsion of (a) PEDOT/MnO$_2$, (b) SW-Fe$_2$O$_3$/MnO$_2$ and (c) SW/MnO$_2$ micromotors in wastewater. Bottom part shows the SEM images of the outer morphology of each micromotors. (B) Influence of the hydrogen peroxide concentration on the speed of each micromotor using 1% sodium cholate as surfactant. (C) Effect different surfactants on the speed of SW-Fe$_2$O$_3$/MnO$_2$ micromotors at a 2% H$_2$O$_2$ concentration. Scale bars, 5 μm (microscopy images) and 1 μm (SEM images).
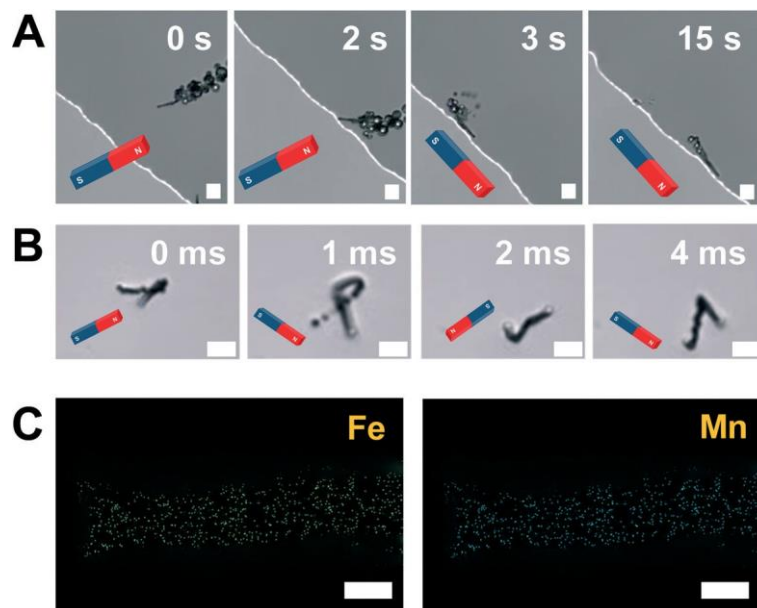

Fig. 4 Magnetic control/actuation of SW-Fe$_2$O$_3$/MnO$_2$ micromotors. (A) Time-lapse microscopy images over 15 s period (taken from Video S2†) showing the navigation of a micromotor toward an area with a high magnetic field. (B) Time-lapse microscopy images (taken from Video S2†) of the magnetic control of the navigation of the micromotors. (C) EDX mapping showing the distribution of Fe and Mn of a SW-Fe$_2$O$_3$/MnO$_2$ micromotor after 60 min navigation in wastewater containing 2% H$_2$O$_2$ and 0.5% of Tween 20. Scale bars, 20 μm (microscopy images) and 2 μm (EDX images).
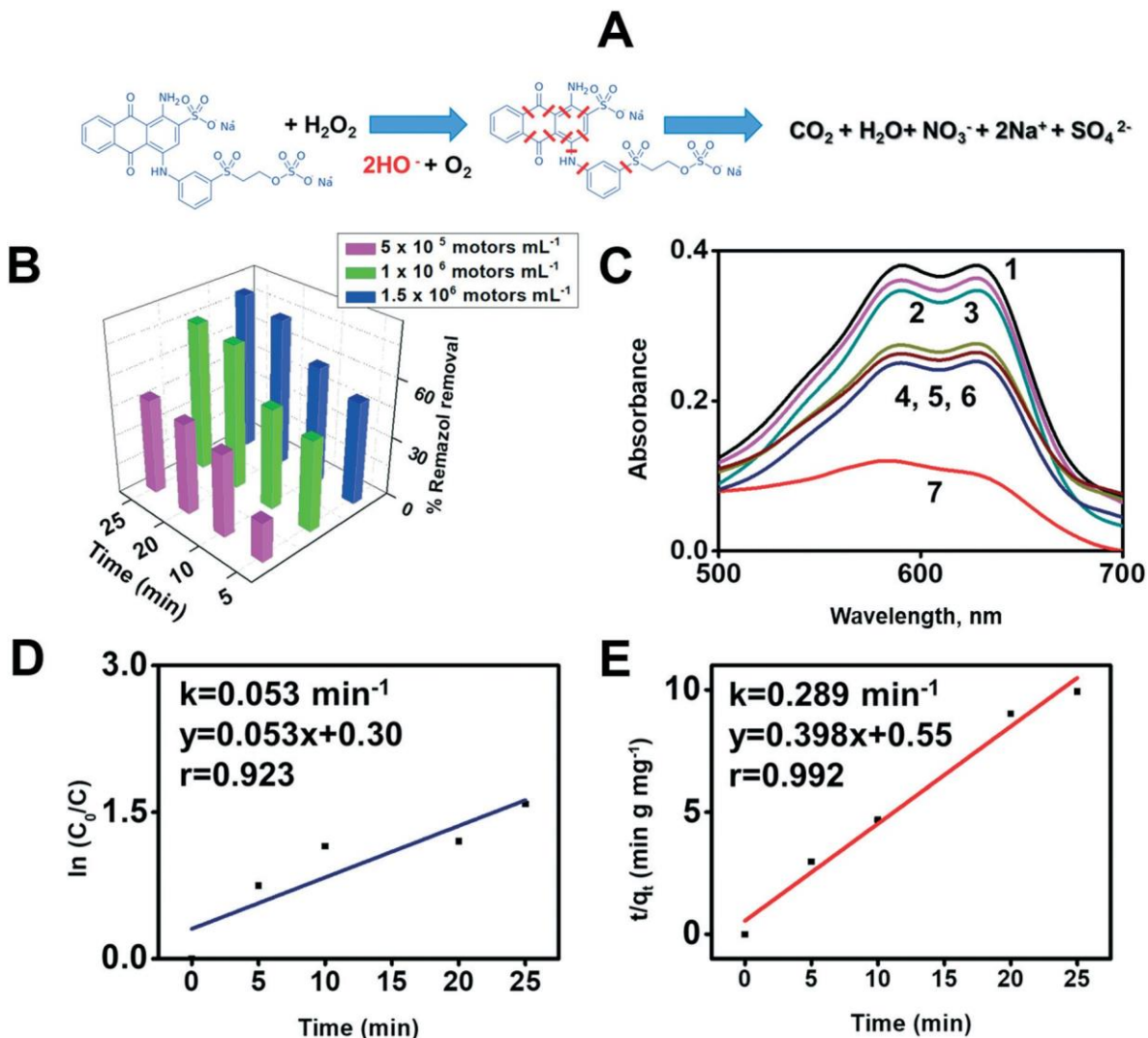
Fig. 5 Advanced oxidation of Remazol Brilliant Blue R (RBB) in wastewater using SW-Fe_2O_3/MnO_2 micromotors. (A) Schematic of the proposed degradation mechanism and pathways. (B) Effect of time and number of motors on the removal efficiency. (C) Absorbance spectra of RBB ($C_0 = 19$ mg L^{-1}) before and after 30 min treatment with the micromotors and control experiments: 1, remazol; 2, static SW-Fe_2O_3/MnO_2 micromotors; 3, moving SW/PtNPs micromotors; 4, moving PEDOT/MnO_2 micromotors; 5, Fe_2O_3 nanoparticles; 6, MnO_2 nanoparticles; 7, moving SW-Fe_2O_3/MnO_2 micromotors. (D) Pseudo-first-order and (E) pseudo-second-order kinetic models for RBB degradation. Conditions: 1% H_2O_2 and 0.5% Tween 20.
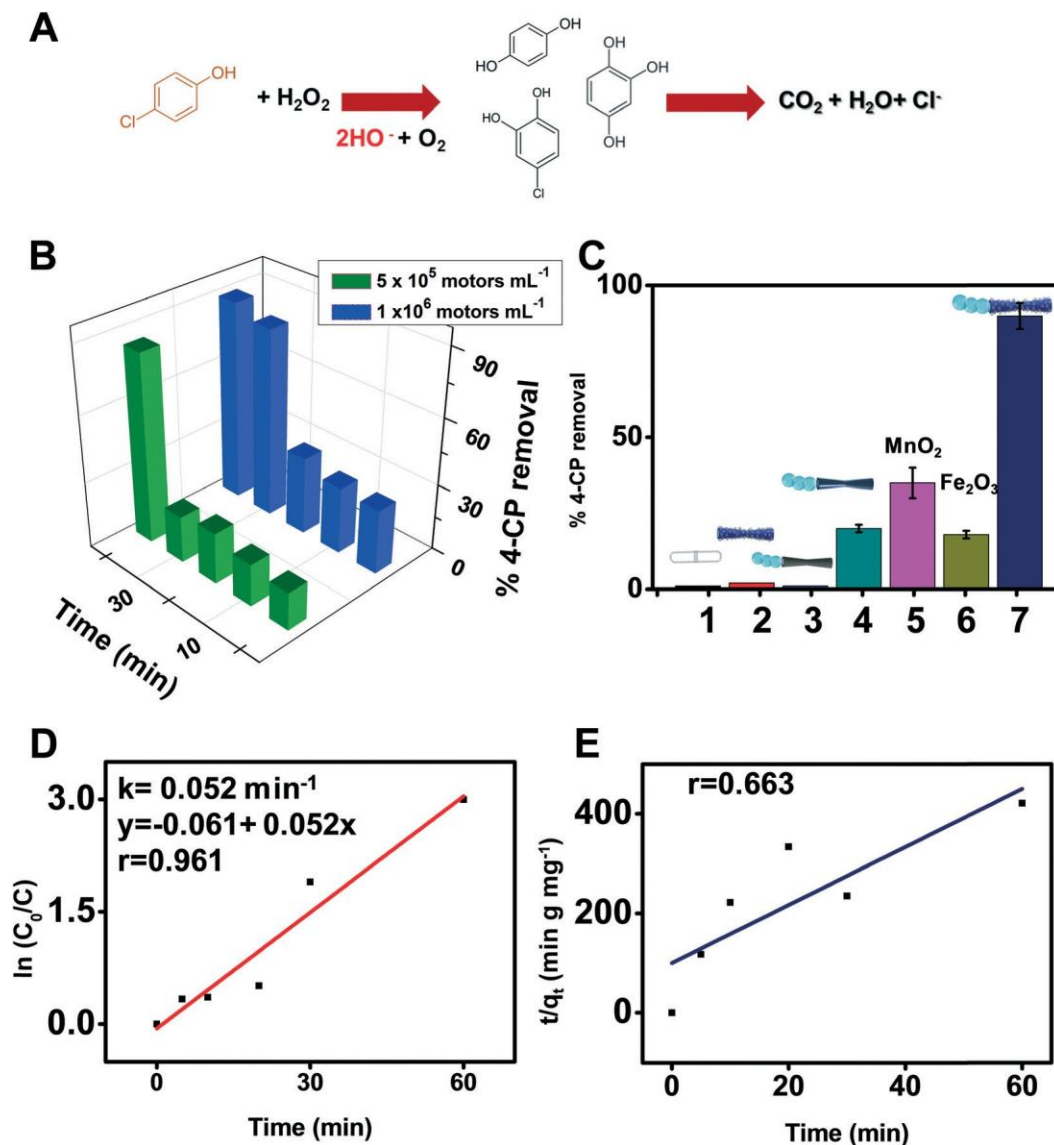
Fig. 6 Advanced oxidation of 4-chlorophenol (4-CP) in wastewater using SW-Fe$_2$O$_3$/MnO$_2$ micromotors. (A) Schematic of the proposed degradation mechanism. (B) Effect of time and number of motors on the removal efficiency. (C) 4-CP removal with micromotors and control experiments: 1, static SW-Fe$_2$O$_3$/MnO$_2$ micromotors with magnetic stirring; 2, static SW-Fe$_2$O$_3$/MnO$_2$ micromotors; 3, moving SW/PtNPs micromotors; 4, moving PEDOT/MnO$_2$ micromotors; 5, MnO$_2$ nanoparticles; 6, Fe$_2$O$_3$ nanoparticles; 7, moving SW-Fe$_2$O$_3$/MnO$_2$ micromotors. (D) Pseudo-first-order and (E) pseudo-second-order kinetic models (right) for 4-CP degradation. Conditions: 1% H$_2$O$_2$ and 0.5% Tween 20